remote sensing

MDPI

Article

The Stability Analysis of Mt. Gongga Glaciers Affected by the 2022 Luding M_S 6.8 Earthquake Based on LuTan-1 and Sentinel-1 Data

Hao Li [1], Bingquan Li [2], Yongsheng Li [1,*] and Huizhi Duan [1]

[1] National Institute of Natural Hazards, Ministry of Emergency Management of China, Beijing 100085, China; lihao2111@mails.ucas.ac.cn (H.L.); duanhuizhi20@mails.ucas.ac.cn (H.D.)
[2] School of Automation, China University of Geoscience, Wuhan 430074, China; bingquanli@cug.edu.cn
* Correspondence: yongshengli@ninhm.ac.cn

Abstract: On 5 September 2022, an M_S 6.8 earthquake occurred in Luding county, Sichuan province, China, with the epicenter located approximately 20 km from the main peak of Mount (Mt.) Gongga. The dynamic situation of Mt. Gongga glaciers has received widespread attention. In this study, Mt. Gongga was selected as the study area, and L-band LuTan-1 (LT-1) satellite data were used for differential interferometric synthetic aperture radar (D-InSAR) processing to obtain the coseismic landform in Luding. Based on Sentinel-1A images, pixel offset tracking (POT) technology was used to obtain the surface movement velocities of the glaciers before, during, and after the earthquake. The results showed that the overall preseismic movement of the glaciers was fast in the area where the ice cascade of the Hailuogou Glacier reached a maximum average deformation rate of 0.94 m/d. Moreover, time-series monitoring of the postseismic glaciers showed that the surface flow velocities of some glaciers in the study area increased after the earthquake. The flow velocity at the main peak of Mt. Gongga and the tongue of the Mozigou Glacier accelerated for a period after the earthquake. The study concluded that the earthquake was one of the direct causes of the increase in glacier flow velocity, which returned to a stable state more than 70 days after the earthquake. The relevant monitoring results and research data can provide a reference for earthquake-triggered glacial hazards and indicate the effectiveness of LT-1 in identifying and monitoring geological hazards.

Keywords: Luding earthquake; Mount Gongga; glacier; LuTan-1; pixel offset tracking

Citation: Li, H.; Li, B.; Li, Y.; Duan, H. The Stability Analysis of Mt. Gongga Glaciers Affected by the 2022 Luding M_S 6.8 Earthquake Based on LuTan-1 and Sentinel-1 Data. *Remote Sens.* **2023**, *15*, 3882. https://doi.org/10.3390/rs15153882

Academic Editors: Yi Wang, Jun Hu and Weile Li

Received: 26 May 2023
Revised: 27 July 2023
Accepted: 3 August 2023
Published: 5 August 2023

1. Introduction

On 5 September 2022, an M_S 6.8 earthquake occurred in Luding county, Sichuan province, China, with the epicenter located in the town of Moxi, Luding county (29.59°N, 102.08°E), at a focal depth of 16 km (China Earthquake Networks Center, https://www.cenc.ac.cn/ (accessed on 8 September 2022)). The seismic intensity map subsequently published by the Ministry of Emergency Management of China for the Luding M_S 6.8 earthquake showed that its highest intensity was nine degrees, with the long axis of the coseismic line trending northwest and the zone with six degrees and above covering an area of 19,089 km^2 [1,2]. This earthquake was a mainshock–aftershock type triggered by the southeast section of the Xianshuihe fault zone, which is a large left-slip fault in the eastern part of the Qinghai–Tibet Plateau in China consisting of nine branching ruptures and connected with the Anninghe fault in Kangding in the south and the Ganzi–Yushu fault in Donggu and Ganzi in the north [3]. It is one of the fault zones with the strongest deformation due to crustal movement in China. This fault zone has historically had strong seismicity, with 23 moderate to strong earthquakes of Ms $\geq$ 6.0 occurring in the Xianshuihe fault zone since 1725 [4,5].

Since the epicenter of the Luding earthquake was adjacent to the Hailuogou scenic area on the eastern slope of Mount (Mt.) Gongga, the impact of the earthquake on the

glaciers of Mt. Gongga has received wide attention. At present, the technical approaches for glacier dynamic monitoring are mainly based on optical and radar remote sensing image interpretation and analysis. Optical images have the advantages of wide coverage and many data sources and are less influenced by topography [6]. However, in the cloudy area of southeastern Tibet, China, it is difficult to accurately quantify the glacier motion field from optical images. In contrast, radar remote sensing has outstanding technical advantages, such as high spatial resolution, independence from climatic conditions, and highly accurate surface deformation extraction, which can effectively compensate for the deficiencies of optical remote sensing. As early as 2002, Strozzi et al. demonstrated the feasibility of the pixel offset tracking (POT) algorithm in a study of glacier motion extraction based on intensity tracking and coherence tracking to estimate the motion of glacier surfaces in the range and azimuth directions with two synthetic aperture radar (SAR) images, and then other scholars adopted the POT method to extract glacier flow velocity [7]. In recent years, satellite SAR remote sensing has shown excellent application prospects for the monitoring of large-scale deformation (including glacier motion) and surface cover changes and has gradually become an important technical approach for the study of the cryosphere and related fields [8–11].

In this paper, the Mt. Gongga glaciers were selected as the research objects, and LuTan-1 (LT-1) and Sentinel-1A satellite SAR images acquired before and after the earthquake were used as the data source. Through differential interferometric SAR (D-InSAR), POT, POT stacking, and POT-SBAS, the motion velocity changes in the Mt. Gongga glaciers before and after the earthquake were analyzed. The evolution of glacier movement at different temporal and spatial scales was identified, and near real-time monitoring and time-series evolution analysis were performed for key deformation areas to provide a reference for the risk assessment of secondary glacial debris flows, landslides, and other disasters caused by the Luding earthquake.

2. Geological Background of the Study Area

The Mt. Gongga region (29°30′–30°20′N, 101°30′–102°15′E) is located at the southeastern edge of the Tibetan Plateau, in the middle of the transition from the Sichuan Basin to the Tibetan Plateau [12,13]. It is one of the areas with the highest concentration of modern glaciers in the Hengduan Mountains. The main peak of Mt. Gongga is 7556 m high [14,15]. The high-elevation area has abundant rainfall, which is conducive to the development of monsoon marine valley glacier topography. There are 74 modern glaciers located in the region of Mt. Gongga, which are radially distributed around the main peak [16]. The total area of the glaciers is 255.1 km^2, and most glaciers are distributed in the southern and eastern parts of the basin [17]. Ridge lines, narrow upper edges, and ridges of hills that can separate large areas of glaciers to form separate specific glaciers flow in different directions. The main ridges of Mt. Gongga extend roughly from north to south. In terms of glacier distribution, the southern part of Mt. Gongga has significantly more glacier cover than the northern part. The direction of water vapor transport makes the eastern slope of Mt. Gongga more humid than the western slope with larger mountain glaciers, such as Hailuogou Glacier, Mozigou Glacier, Yanzigou Glacier, and Nanmenguanogou Glacier [18]. The glaciers on the western slope are more numerous but smaller in scale, with representative glaciers being Dagongba Glacier and Xiaogongba Glacier. The epicenter of the Luding earthquake and the regional distribution of the major fault zones are shown in Figure 1.

Ice avalanches are a typical glacial hazard, and their frequency and scale are related to climate change and associated with glacier surges, glacial fracture disintegration, and regional earthquakes. Under certain conditions, catastrophic ice avalanches may induce ice avalanche-induced debris flow chains, forming an isolated catastrophic effect. Mt. Gongga is the largest active marine glacier area in the southeastern margin of the Hengduan Mountain system and the Tibetan Plateau and the largest modern glacier concentration center in Sichuan. The glacier and its surrounding moraine are very large in mass and

located at a high elevation. Glacier debris flows, glacier outburst floods, landslides, and other disasters caused by moving glaciers are extremely destructive, posing a serious threat to the safety and property of residents in the surrounding and downstream basins and the stable operation of infrastructure. Therefore, the dynamic monitoring of glacier movements after earthquakes can effectively reflect their dynamic evolution and is of great significance for mountain disaster early warnings and forecasting.

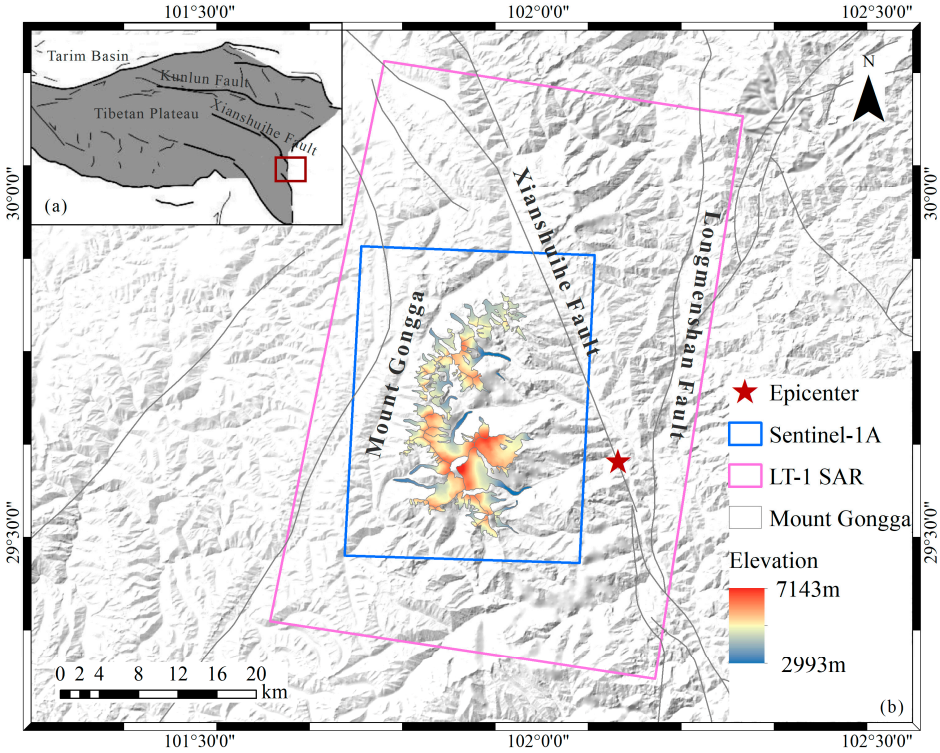

Figure 1. Study area and coverage of satellite SAR images. (**a**) A sketch of the tectonic background of the Qinghai–Tibetan Plateau and adjacent areas; (**b**) regional tectonic background of the 5 September 2022 M_S 6.8 Luding earthquake. The gray polygon indicates the area of Mt. Gongga extracted from the Second Glacier Inventory of China version 1 [19]. The blue polygon shows the coverage area of the cropped Sentinel-1A images. The magenta polygon shows the coverage area of the cropped LT-1 SAR images.

3. Data and Methods

3.1. Data

Sentinel-1 is an Earth monitoring satellite with C-band SAR launched by the European Space Agency (ESA) to provide all-time and all-weather images (https://www.esa.int/ (accessed on 9 January 2023)). The Sentinel-1 satellite mostly acquires large-scale and wide-range SAR data in TOPS imaging mode. It is widely used in the extraction and analysis of large-scale glacier movements due to its short revisit period, wide coverage area, and free and easy access to data [20]. In this paper, we use ascending track SAR data acquired from the Sentinel-1A satellite from 12 September 2021 to 5 January 2023 with a spatial resolution of 2.33 m × 13.97 m and a revisit period of 12 d.

LT-1 consists of two advanced full-polarization L-band radar satellites, LT-1 A and LT-1 B. Satellite A was launched on 26 January 2022, and satellite B was launched on 27 February of the same year. The satellite constellation supports two imaging modes. The bistatic InSAR mode is implemented to produce a digital elevation model (DEM) with high accuracy and spatial resolution. The monostatic mode is implemented by having the satellites follow each other in flight with a 180° orbital phasing difference to shorten the revisit time to 4 days, allowing the use of D-InSAR technology to measure terrain changes at large scales with millimeter accuracy [21–23]. The LT-1 SAR makes full use of the characteristics of

the long L-band radar's wavelength and penetrating ability in vegetated areas, which can provide longwave SAR data with wide coverage, a high density of measurement points, and a high frequency of repeated observations for early identification of hazards. In this paper, preseismic and postseismic interferometric image pairs acquired by the LT-1 SAR satellite on 4 September and 12 September 2022 are used to study the influence of earthquakes on the evolution of glacier motion on Mt. Gongga. The detailed acquisition parameters for these two SAR data stacks are listed in Table 1, with their coverages shown in the inset map in Figure 1.

Table 1. Main parameters of the satellite data used in this study.

	Sentinel-1A	**LuTan-1**
Polarization mode	VV	HH
Orbit mode	Ascending	Descending
Radar wavelength (cm)	5.6 (C-band)	23.8 (L-band)

3.2. Method

The POT technique does not require phase decoupling, can overcome problems such as negative correlation, and is widely used in the monitoring of large-gradient surface deformation, such as glacier flow, landslide displacement, and seismic deformation fields [24]. Additionally, with the small-baseline subset (SBAS) technique, deformation time-series results are obtained through the combination of spatiotemporal baselines formed by two baseline constraints in time and space. The research process is shown in Figure 2 and contains three key steps: (1) obtaining the range-oriented displacement using the POT technique; (2) applying the POT-SBAS technique; and (3) implementing the POT-stacking technique.

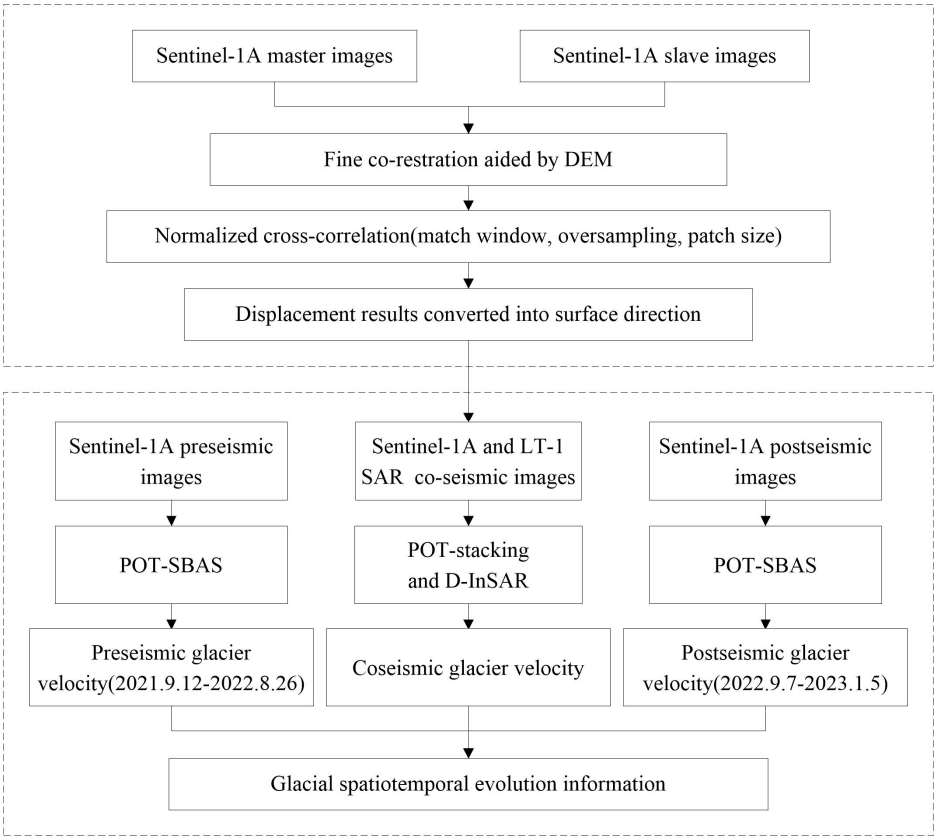

Figure 2. The workflow of the study.

3.2.1. Pixel Offset Tracking

POT technology is used to estimate satellite orbit offset and surface deformation offset by correlating SAR images from two different periods in a correlation window. The POT method applies the normalized cross-correlation (NCC) to calculate the azimuthal and range offsets [25]. The formula is as follows.

$$NCC(\mu, \nu) = \frac{\sum_{x,y} (f(x,y) - f_r)(g(x+\mu, y+\nu) - g_s)}{\sqrt{\sum_{x,y} (f(x,y) - f_r)^2} \sqrt{\sum_{x,y} (g(x+\mu, y+\nu) - g_s)^2}} \quad (1)$$

where (x, y) is the center coordinate of the template window, (μ, ν) indicates the center coordinate of the search window, f_r is the average pixel value of the template window, and g_s is the average pixel value of the search window. When the $NCC(\mu, \nu)$ value is closer to 1, the similarity between the two images is greater. When the cross-correlation coefficient is at the maximum, it indicates that the registration of the two images is complete. Therefore, the offset between the template window and the search window can be calculated. The calculation formula is as follows.

$$D_{offset} = D_{defo} + D_{orbit} + D_{topo} + D_{ionos} + D_{noise} \quad (2)$$

where D_{offset} is the offset obtained after registration and D_{defo} is the offset due to surface deformation. D_{orbit} is the offset due to flight orbit and satellite attitude, which can be removed by fitting a bilinear polynomial to the geometric transformation parameters. D_{topo} is the offset due to terrain undulation. D_{ionos} is the ionospheric offset, which is negligible at low and middle latitudes where the ionospheric influence is small. D_{noise} is the offset due to system noise, which is negligible. This method relies on speckle features in SAR images, which can overcome the problem of low-coherence or even incoherent images and is more suitable for glacial areas.

3.2.2. POT-SBAS

Traditional POT technology is generally limited to processing with two images. It is often difficult to obtain the temporal characteristics of glacier motion and unexpected conditions, such as glacier surges. With the POT-SBAS technique and monitoring points with better stability on the glacier surface, the frequency of motion monitoring can be increased to better reflect the spatial and temporal evolutionary characteristics of glacier motion [26]. The monitoring of the spatiotemporal evolution of glacier motion with the help of the POT-SBAS technique relies on the optimal baseline combination of the SBAS method to add redundant observations. Then, with the help of singular value decomposition (SVD) and other methods, the effect of noise can be further reduced [27]. Assuming that the range direction displacements of M image pairs corresponding to $N+1$ SAR acquisition moments are acquired, the following observations are available:

$$\delta N = [\delta d_{N1} ... \delta d_{NM}]^T \quad (3)$$

$\delta d_{Ni} (i = 1, ..., M)$ is the displacement value corresponding to any set of image pairs in the upward range direction. The time series corresponding to the master and slave images are

$$D_m = [D_{m1}, ..., D_{m1M}] \quad (4)$$

$$D_s = [D_{s1}, ..., D_{s1M}] \quad (5)$$

Arranged in time order, D_{mi} is earlier than $D_{si} (i = 1, ..., M)$, and the time interval of the M image pairs is expressed as

$$\delta N_j = d(t_{Dmj}) - d(t_{Dsj}) (j = 1, ..., M) \quad (6)$$

The equation is an M equation with N unknowns; written in matrix form, it appears as follows:

$$\delta N = Ad \tag{7}$$

Each row of the A matrix corresponds to an image pair, and each column corresponds to one SAR image. The displacement value d for each time in the line of sight (LOS) can be obtained by using SVD. Based on the POT-SBAS technique, this paper obtains the offset tracking results for the corresponding combinations through the combination of spatiotemporal baselines formed by two baseline constraints in time and space, and on this basis, the time-series information for the glacier surface motion is obtained by inversion.

3.2.3. POT-Stacking

The POT-stacking technique assumes that the surface deformation in the study area is mainly linear [28]. The advantage is that the calculation is efficient and the influence of random errors can be effectively reduced. The POT-stacking technique obtains multiple POT deformation results by controlling the spatiotemporal baseline with multiple master images and accumulates the deformation results to effectively solve the temporal and spatial decoherence problems [29]. It is one of the methods that can be used to effectively improve the accuracy of the POT deformation solution. It is easy to portray the morphological characteristics of significant deformation areas in the POT deformation fields. In this paper, the LS is used to average the POT deformation fields, and the POT maps are weighted by time intervals to obtain the LOS-oriented deformation rate for the study area, which is calculated as

$$\varphi_{rate} = \sum_{i=1}^{N} \Delta t_i \varphi_i / \sum_{i=1}^{N} \Delta t_i^2 \tag{8}$$

where Δt_i is the time interval for the POT results of a group i; φ_i is the POT deformation for a pair i; Δt is the time baseline for the POT pairs; and N is the number of POT image pairs.

4. Results

4.1. Coseismic Displacements Derived from the LT-1 SAR

In this paper, traditional D-InSAR is used to process strip-mode LT-1 SAR images to obtain the InSAR coseismic LOS surface deformation field of the 2022 Luding earthquake (as shown in Figure 3). To improve the signal-to-noise ratio, 5:5 (range: azimuth) multi-look and Goldstein filter processing are adopted for the LT-1 SAR image data [30,31]. The minimum cost flow (MCF) algorithm is then used to unwrap the phase. The spatial distribution and magnitude of the deformation caused by the Luding earthquake can be clearly described based on the coseismic deformation field [32–34]. The results show that the earthquake was located in Moxi town at the tail end of the Xianshuihe fault. Its motion direction gradually spread southward from northwest to southeast, and the motion mode also gradually shifted from left-slip motion to mainly slip motion with a recoil component. The horizontal motion of the surface on the west side of the fault was projected in the LOS direction as a lifting signal. In general, the deformation distribution characteristics of the InSAR were consistent with the nature of left-slip motion. On the west side of the seismogenic fault (Xianshuihe fault), the positive deformation signals in the satellite LOS direction reached 20 cm, and on the east side of the fault, the deformation in the LOS direction reached −25 cm. The range of surface deformation caused by the earthquake was approximately 900 km^2. At the same time, multiple local deformation signals were found around the epicenter, due to the landslide and glacier movement triggered by the earthquake, with the L-band sensor of LT-1, which can capture signals of larger deformation gradients.

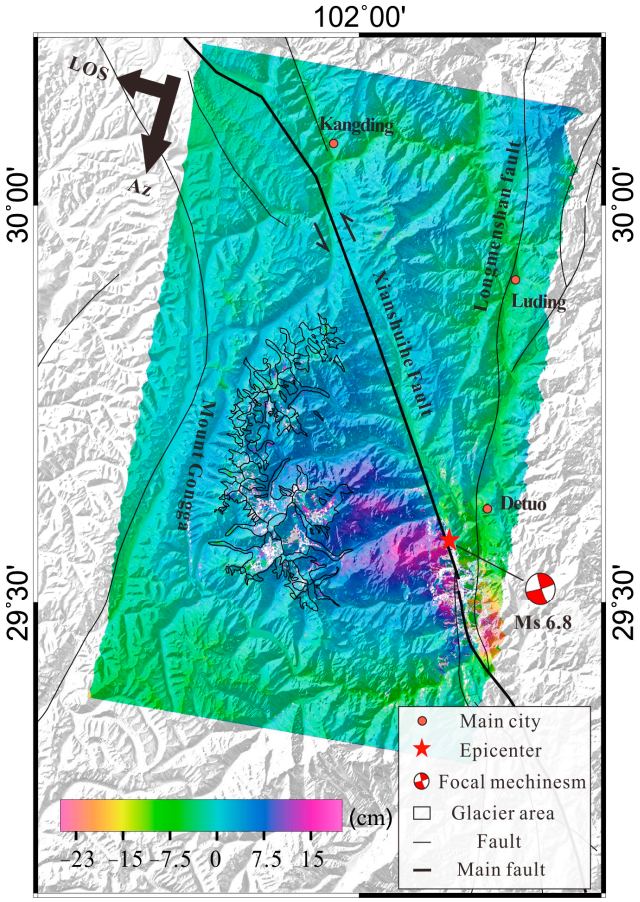

Figure 3. Coseismic surface displacements in the LOS direction for the 2022 Luding earthquake.

4.2. Dynamic Feature Monitoring of Glacier Movement Based on Sentinel-1

To verify the effect of the Luding earthquake on the surface velocity of Mt. Gongga glaciers, Sentinel-1A data covering the study area from 12 September 2021 to 5 January 2023 were used for POT processing. 26 August 2022 and 7 September 2022 were used as the cutoff points to obtain the Mt. Gongga glacier surface flow velocities before, during, and after the earthquake. A long-term POT time-series analysis of the characteristics of glacier movement after the earthquake was conducted to further explore the evolution of glacier movement and the impact of earthquakes. To reduce the problem of errors due to inconsistent time intervals, the calculated results were uniformly converted into units of days for intercomparison. Due to the low accuracy of the POT method based on Sentinel-1A multiperiod data in the azimuthal direction, only the flow velocities in the range direction of the glaciers in Mt. Gongga were analyzed.

4.2.1. Preseismic

Sentinel-1A images from 12 September 2021 to 26 August 2022 were selected to calculate the glacier surface flow deformation rate based on the POT to reveal the long-term slow deformation of glaciers not triggered by earthquakes. Figure 4 shows the preseismic POT daily average deformation rate results. Negative values indicate glacier movement in the opposite direction along the radar LOS. From the monitoring results, the range displacement distribution before the earthquake generally showed movement along the track direction. The accumulation area of Hailuogou Glacier, the ice tongue of Mozigou Glacier, and the trailing edge of Yanzigou Glacier were the most obvious. The maximum velocity of the glaciers along the track direction was 0.94 m/d, and the velocity of the glaciers against the track direction was approximately −0.1 m/d. The maximum value for the glaciers along the track direction was obtained for Hailuogou Glacier No. 1. The

detailed names of each part of Hailuogou Glacier No. 1 are shown in Figure 5. The velocity difference between the glacier accumulation area and the ablation area was significant. There are three areas with higher flow velocities in the firn basin, and the average velocity is approximately 0.8 m/d. The three glacier tributaries developed from the firn basin converge in the connection area between the ice waterfall and the top of the ice tongue, with a flow velocity of approximately 0.7 m/d. In recent years, because of global warming, the melting of glaciers has accelerated, and their thickness has continued to decrease. The ice waterfall and ice tongue of Hailuogou Glacier No. 1 have been completely disconnected, forming a cliff area with a height difference of approximately 1000 m. The glaciers accumulated in the relatively wide and gentle firn basin concentrate downward from all directions and gather at the narrow and long valley section at the top of the ice waterfall. Due to the steep slope of the terrain and the exposed front edge of the glacier, the flow velocity here increases significantly. Liu et al. used 38 PALSAR-1/2 images collected from 2007 to 2018 and POT to obtain glacier deformation velocities and found three areas with higher transport velocities in the firn basin of Hailuogou Glacier No. 1, which are consistent with the range obtained in this study.

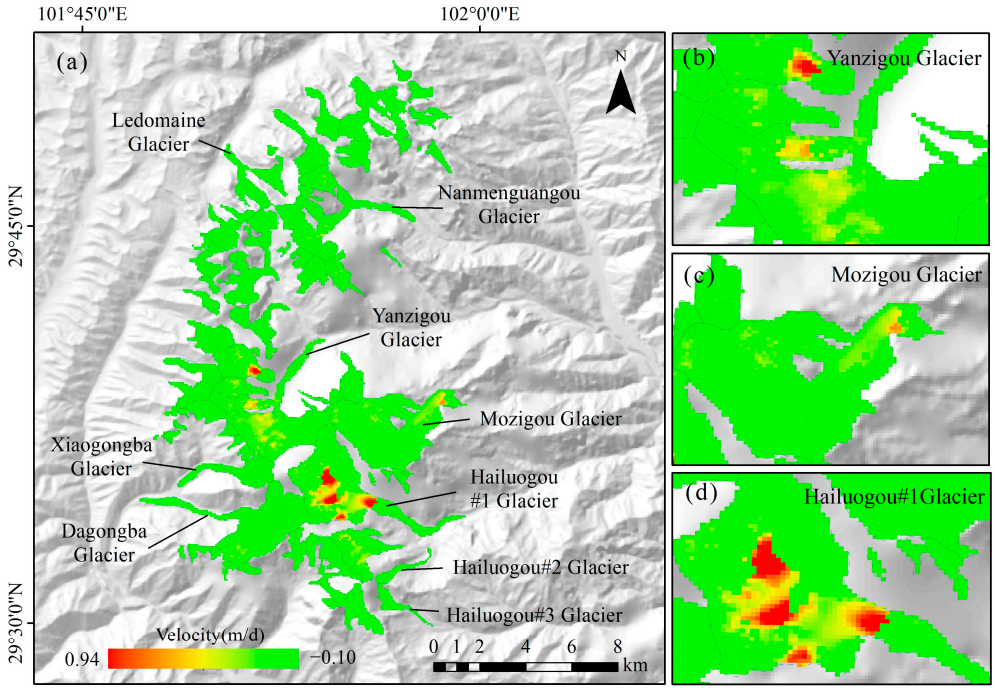

Figure 4. (**a**) The surface velocity of the Mt. Gongga glacier from 12 September 2021 to 26 August 2022 in the radar line-of-sight direction; (**b**) localized surface velocity of Yanzigou Glacier; (**c**) localized surface velocity of Mozigou Glacier; (**d**) localized surface velocity of Hailuogou Glacier No. 1.

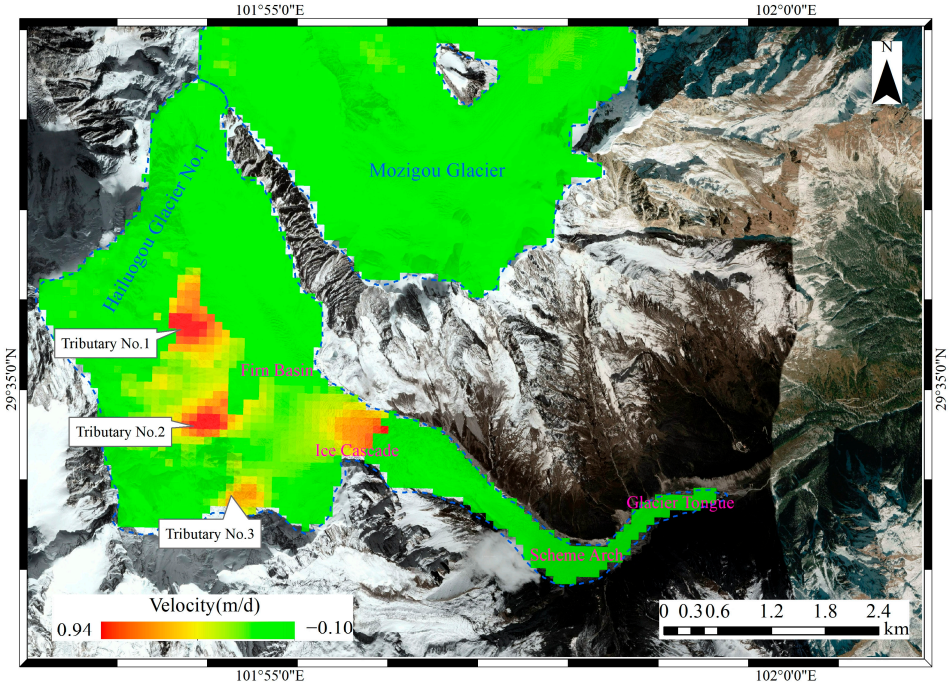

Figure 5. Geomorphologic map of Hailuogou Glacier No. 1 on the eastern slope of Mt. Gongga, southeastern Tibetan Plateau (background image: © Google Earth, 5 October 2020). The blue dotted line indicates the boundary between Hailuogou Glacier No. 1 and the Mozigou Glacier. The solid border indicates the three fast-moving tributaries of Hailuogou Glacier No. 1.

4.2.2. Coseismic

Two scenes of Sentinel-1A images (26 August 2022 and 7 September 2022) covering the earthquake were selected to produce the coseismic glacier deformation map for the Luding earthquake based on POT stacking. Figure 6 shows the POT daily average rate results for the two scenes of images before and after the Luding earthquake. The glaciers with more drastic coseismic velocity changes were Hailuogou Glaciers Nos 1–3 on the eastern side of Mt. Gongga. The Mozigou Glacier and its trailing mountains also showed obvious deformation, while the glaciers on the west side of the ridge line were relatively less affected by the earthquake. The glacier flow velocity on the eastern slope of Mt. Gongga is mostly along the track direction, and the maximum value for the movement along the track direction is approximately 1.5 m/d, the velocity of the movement against the track direction is approximately −0.9 m/d, and the overall movement is along the track direction. The most obvious flow velocity is that of Hailuogou Glacier No. 1, where the deformation at its end in the ice waterfall area from 3700 m to 4980 m above sea level is the most significant, and the flow velocity of the glacier surface is approximately 1 m/d.

The accuracy of the monitoring results was affected by the presence of some null values in the processing results from the Sentinel-1A images. Therefore, the differential interferometry results from the LT-1 satellite were compared and analyzed. Influenced by the SAR observation angle and the geometric relationships of the topographic relief, most of the western side of the ridgeline showed subsidence, while the eastern side of the glaciers mostly showed uplift (movement to the east), and the end of the glaciers was where the most drastic changes occurred. There were several areas with obvious deformation signals on the surface of the Mt. Gongga glaciers, which were suspected to be glacial mudflows and landslides. This reflects the advantages of using L-band SAR data in the study of glacier movement velocity.

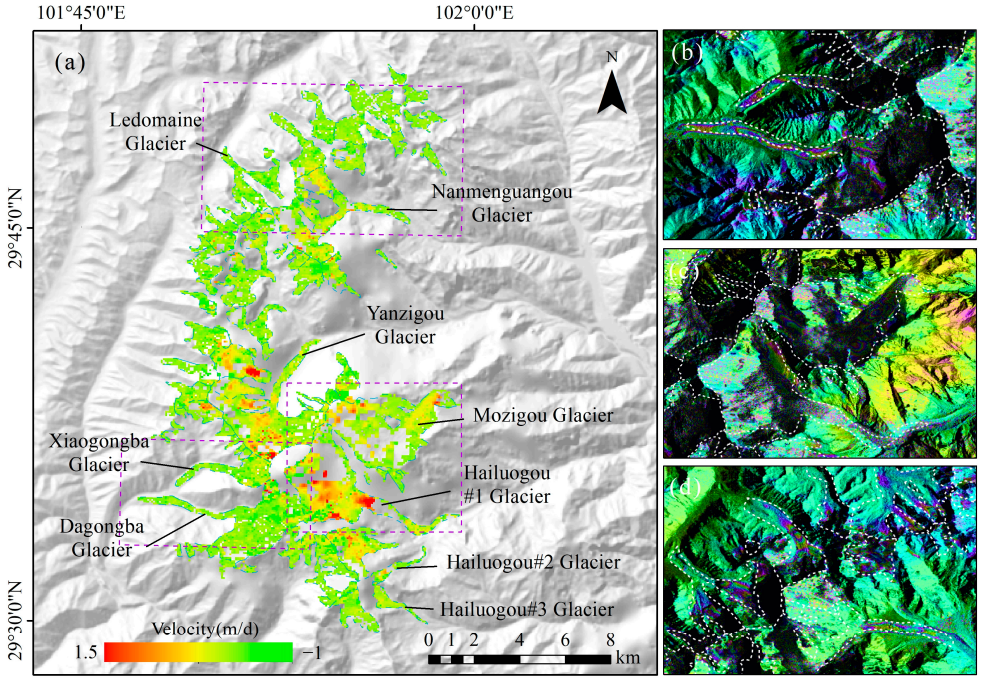

Figure 6. The POT deformation results. (**a**) Sentinel-1A SAR images between 26 August and 7 September 2022; (**b**–**d**) LT-1 SAR image coseismic surface displacements between 4 September and 12 September 2022.

4.2.3. Postseismic

Based on POT technology, this article presents the average deformation rate four months after the Luding M_S 6.8 earthquake (Figure 7). As shown in Figure 7, there are also large-scale glaciers still moving along the track after the earthquake. The epicenter of the Luding earthquake was near Hailuogou Glacier No. 1, close to three large modern glaciers on the eastern slope of Mt. Gongga (less than 10 km in a straight line from both Hailuogou and Mozigou Glaciers and less than 20 km from the ice tongue of Yanzigou Glacier). The glaciers and periglacial areas more actively affected by the earthquake were concentrated in the central and southern parts of the main peak. The accumulation area of Hailuogou Glacier No. 1, the trailing edge of Hailuogou Glacier No. 2, the upper reaches of Mozigou Glacier, and the main peak of Mt. Gongga were affected by the Luting earthquake with drastic displacement changes. The maximum flow velocities in the positive and negative LOS directions were 3.3 and −0.9 m/d, higher than the average velocities before the earthquake. The average postseismic velocity in three areas of Hailuogou Glacier No. 1 in the firn basin reached 2.5 m/d and that in local areas could reach 3 m/d. The flow velocity at the junction between the upper edge of the ice waterfall and the firn basin could reach 2 m/d, twice the average flow velocity before the earthquake.

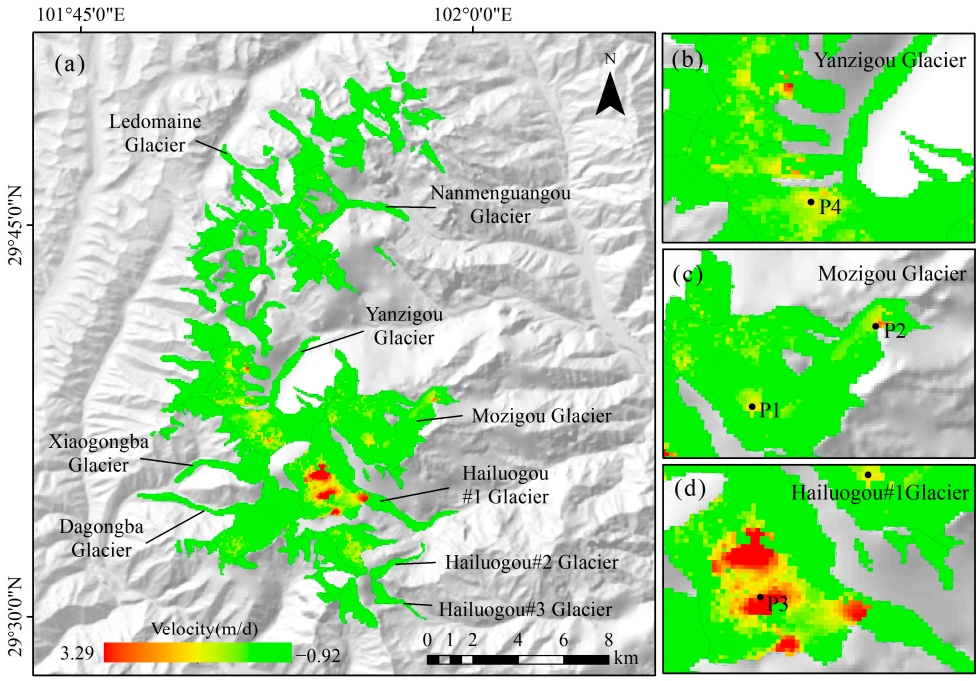

Figure 7. (**a**) The POT deformation results from Sentinel-1A SAR images between 7 September 2022 and 5 January 2023; (**b**) localized surface velocity of Yanzigou Glacier; (**c**) localized surface velocity of Mozigou Glacier; (**d**) localized surface velocity of Hailuogou Glacier No. 1.

To further investigate the effects of the earthquake on the morphology of some of the glaciers in the study area, four selected points were chose at different locations, including Mozigou Glacier, Hailuogou Glacier, and the main peak of Mt. Gongga (see Figure 7; P1, P2, P3, and P4), to carry out postseismic displacement time-series analysis in the study area. Figure 8 shows the time-series evolution for points P1–P4 in the LOS direction, with each point recording the cumulative shape variables four months after the earthquake. The ground deformation at each selected point in the time series based on the cumulative deformation variables showed a gradual increase in the post-earthquake monitoring period. Of these four points, P3 had the largest cumulative deformation of about 73 m. The overall movement trend for the displacement of the four points initially showed an increase in velocity and then a slow increase in surface displacement with time. In addition, there were no visible glacier dynamics anomalies from the temporal displacements of each sample during the selected data collection period, neither in the accumulation zone nor in the ablation zone.

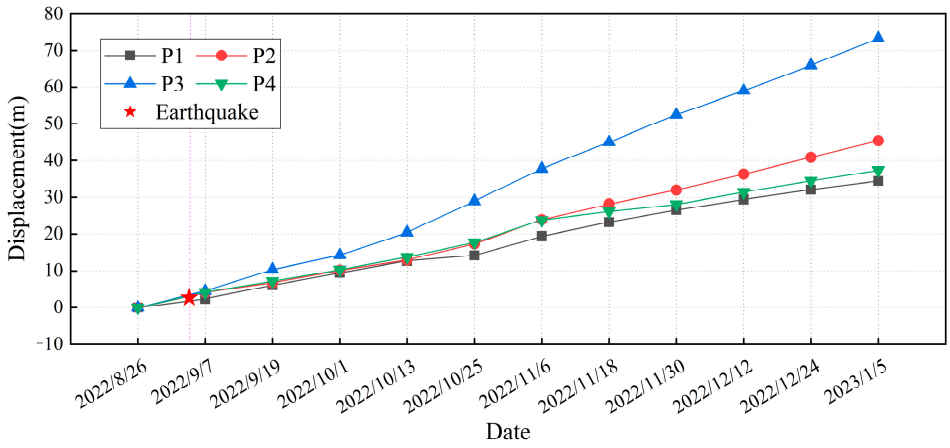

Figure 8. Time-series results for the surface displacement field of the selected sample points.

5. Discussion

5.1. Surface Velocity Changes before and after the Earthquake

The glacier flow velocity monitoring images before and after the earthquake in the local area of the Mt. Gongga glaciers were compared to check whether the earthquake caused changes in the glacier surface geomorphology. As shown in Figure 9, there are significantly more locations with accelerated flow velocities after the earthquake in the same metric. The movement of loose moraine material on the surface of the main peak of Mt. Gongga and the ice waterfall of Hailuogou accelerated. The earthquake is thought to have destabilized the lateral slopes of the Hailuogou Glacier, and no new damage was found on either side of the ice tongue. Many previous studies have shown that, in most cases, earthquakes are only a prerequisite for paraglacial slope damage.

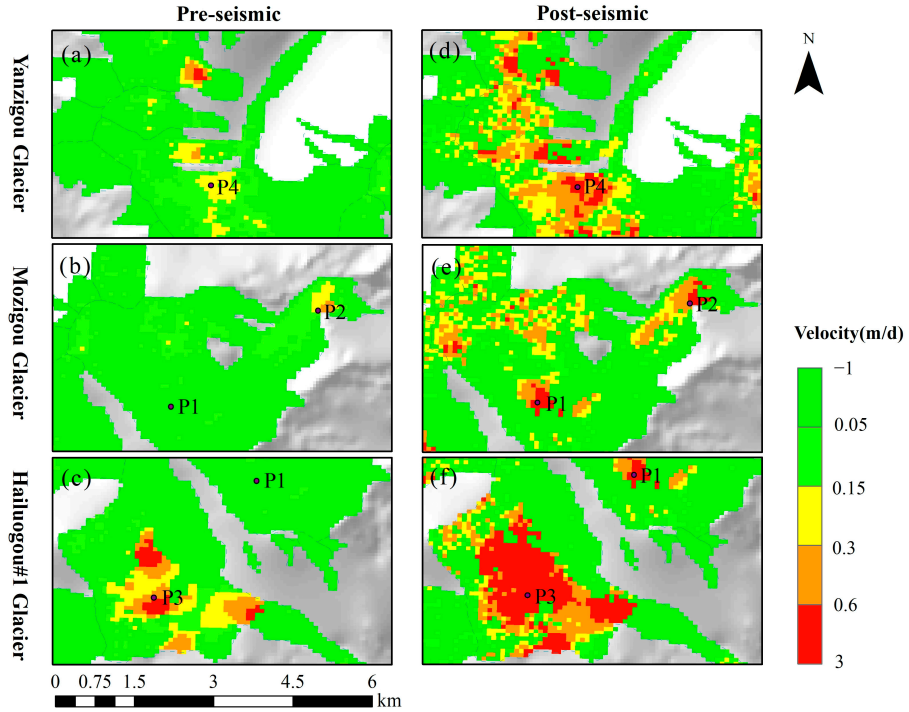

Figure 9. POT deformation results from Sentinel-1 SAR images from different periods. The velocity fields shown in (**a**–**c**) correspond to period from 12 September 2021 to 26 August 2022. The velocity fields shown in (**d**–**f**) correspond to the period from 7 September 2022 and 5 January 2023.

5.2. Comparison of Sentinel-1 and LT-1 in Coseismic Surface Monitoring and Analysis

Li et al. used 14 Sentinel-1A images to determine glacier deformation velocity, 8 of which were taken in 2020 or 2021 to monitor the deformation characteristics of Hailuogou Glacier under nonseismic effects and the remaining 6 of which were taken before and after the 2022 earthquake to evaluate the degree to which Hailuogou Glacier was affected by the earthquake. They found that the earthquake caused glaciers on the eastern side of Mt. Gongga's peaks to deform sharply, including Hailuogou, Mozigou, Yanzigou, Nanmengou, and their hinterland gullies, while the glaciers on the west side were relatively less affected. The icefall deformation in the Hailuogou catchment area was the largest, with a maximum average movement velocity of approximately 2.5 m/d [35]. The coseismic results from this paper showed that the flow velocity of the Hailuogou Glacier reached 1.5 m/d, which was lower than the values reported by Li et al. The low value may have been due to potential ice and snow avalanches on the steep slopes leading to a lack of corresponding pixels in the multitemporal SAR images, thus reducing the signal-to-noise ratio for the estimated POT and affecting the results to a certain extent. In addition, the resolution of the Sentinel-1A data used in this paper was 120 m, which could have impacted the accuracy of the values.

5.3. Glacier Stability and Postseismic Risks

The epicenter of the Luding earthquake was close to the southeastern section of the Xianshuihe fault zone. The Xianshuihe fault is located at the strike-slip boundary between the Bayan Har block and the Sichuan–Yunnan block and intersects with the Longmenshan fault and Anninghe fault to form the famous "Y-shaped" fault zone in western Sichuan [36]. Relevant studies have shown that, under the influence of the Wenchuan and Lushan earthquakes on the Longmenshan fault in 2008 and 2013, the Coulomb stress near the Xianshuihe fault increased significantly, and the strain energy accumulated in the Kangding–Shimian section was released in this earthquake [37]. The fault zone caused the coseismic activity to result in deformation in Mt. Gongga glaciers, and the glacier slip rate changed after the earthquake. In this paper, the glacier slip rate for Mt. Gongga in the short postseismic period is studied. Figure 10 shows the time series for the glacier slip rate at four selected sites (P1–P4) for four months after the earthquake. The numerical values represent the deformation results for each epoch relative to the previous epoch, the null values were averaged over the upper and lower epochs, and the calculated results were converted to units of days for analysis. As shown in Figure 10, the flow rate obtained at point P1 on 7 September 2022 was approximately 0.2 m/d, fluctuating up to 0.45 m/d and then decreasing to the preseismic flow rate. The flow velocities obtained at points P2 and P4 on 7 September 2022 were approximately 0.33 m/d, gradually increasing to 0.55 m/d and 0.5 m/d under the influence of the Luding earthquake and then decreasing to the preseismic flow velocity or slightly above. The flow velocity at point P3 obtained on 7 September 2022 was approximately 0.37 m/d, fluctuating up to 0.73 m/d and then decreasing to 0.6 m/d, slightly higher than the preseismic flow velocity. In general, the postseismic motion rates at all four points showed a trend of obvious acceleration, reaching a peak in early November and then slowly decreasing to the preseismic level.

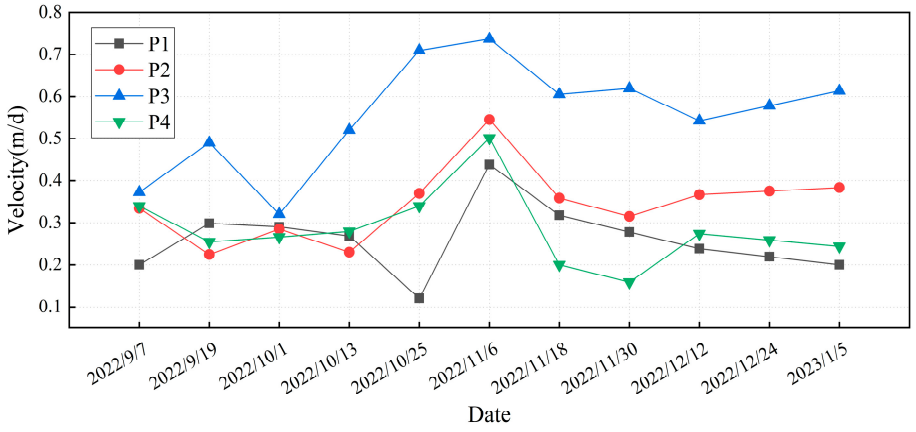

Figure 10. Time-series results for the glacier velocity field at selected sample points.

Generally, postseismic glacier sliding has a large and significant deformation gradient at the early stages and then gradually decays with time. Liu Q. et al. monitored two large-scale ice avalanches on Hailuogou Glacier before the "9.5" Luding earthquake, which were captured by an automated observation camera on 8–9 August and 1–4 September. The ice avalanche that occurred on 8 and 9 August covered an area of 0.17 km^2, and the avalanche distance was 553 m. Between 1 and 4 September, the deposition area was approximately 0.2 km^2, and the avalanche distance was approximately 608 m [18]. These two ice avalanche events may have unloaded a large amount of ice and prevented a larger ice avalanche from being triggered during the earthquake activity. According to the China Seismological Network Center, an M_S 5.0 earthquake occurred on 22 October 2022, Beijing time, in Luding county, Ganzi prefecture (29.61°N, 102.03°E), which was an aftershock of the 2022 Luding earthquake. The increase in flow velocity at each selected in late October is suspected to be influenced by aftershocks, where the relatively stable ice in the upper

icefall flowed rapidly, pushing the ice downstream and causing the glaciers to flow faster. Through the comparative analysis of the movement velocity of the glaciers before and after the earthquake, the preliminary interpretation is that the direct impact of the earthquake on the glaciers was mainly concentrated on the glaciers at the ridge of Mt. Gongga and in Hailuogou, the direct impact on the glaciers at the back edge of Mt. Gongga was small, and a large continuous deformation area has not yet been formed. Generally, the glaciers are still stable. The preliminary conclusion is that the probability of a large-scale ice avalanche event directly causing a disaster after an earthquake is low.

6. Conclusions

Based on the L-band LT-1 satellite and C-band Sentinel-1A data, this paper used D-InSAR and POT methods to obtain the high-precision coseismic surface displacements for the Luding M_S 6.8 earthquake and the surface motion rate for Mt. Gongga and its time-series evolution characteristics.

The rupture of the fault extended along the NNW–SSE direction, and the motion mode was mainly sinistral with a gradual shift to slip-based motion with a thrust component. Uplift signals were evident on the western side of the fault, with maximum LOS uplift and subsidence values of approximately 20 cm and 25 cm, respectively. At the same time, multiple landslide and glacier movement deformation signals triggered by earthquakes were found at the epicenter location, reflecting the advantages of the LT-1 SAR's L-band sensor in monitoring large deformation gradients, such as those due to earthquakes and glaciers. The distribution of POT displacement from the Sentinel-1A before and during the earthquake was generally along the LOS direction. The accumulation area of Hailuogou Glacier, the ice tongue of Mozigou Glacier, and the hills at the back edge of Yanzigou Glacier were the most obvious. The glaciers with more drastic changes in flow velocity during the earthquake were Hailuogou Glaciers Nos 1–3 and Mozigou Glacier and its back-edge mountains on the east side of Mt. Gongga, with the maximum movement along the range direction reaching up to 1.5 m/d. The areas with accelerated glacier flow velocities after the earthquake were mainly found in the accumulation area of Hailuogou Glacier No. 1, the trailing edge of Hailuogou Glacier No. 2, the glacier tongue of Mozigou Glacier, and the main peak of Mt. Gongga.

Through the comparative analysis of the time series for the glacier slip rate of Mt. Gongga glaciers four months after the earthquake, the conclusion was that the earthquake has caused some damage to glacier stability but has not yet formed a continuous large deformation area. The glaciers are still in a stable state, and the probability of a large-scale ice avalanche event directly causing disaster after an earthquake is low. However, the accuracy analysis of glacier surface motion using Sentinel-1 data has some shortcomings. In the future, we will further collect meteorological data and multisource remote sensing data for the glacier area to extend the observation period for glacier surface motion at Mt. Gongga to provide more reliable data support for the analysis of postseismic glacier activity.

Author Contributions: Conceptualization, Y.L. and H.L.; methodology, B.L. and H.L.; software, B.L. and H.D.; validation, Y.L., B.L. and H.D.; formal analysis, H.L.; investigation, H.D.; resources, Y.L.; data curation, B.L. and H.L.; writing—original draft preparation, H.L.; writing—review and editing, Y.L. and B.L.; visualization, H.L.; supervision, Y.L.; project administration, Y.L. and B.L.; funding acquisition, Y.L. All authors have read and agreed to the published version of the manuscript.

Funding: This research was funded by the National Key Research and Development Program of China (grant no. 2021YFC3001903), Science and Technology Program of Tibet Autonomous Region (XZ202301YD0002C-01) and the Alibaba Innovation Research Program (24024696-CRAQ717HZ11230008).

Data Availability Statement: The Sentinel-1 data used in this study were downloaded from the European Space Agency (ESA) through the ASF Data Hub website https://vertex.daac.asf.alaska.edu/ (accessed on 20 January 2023).

Acknowledgments: The authors would like to thank the ESA and ASF for providing the Sentinel-1 data.

Conflicts of Interest: The authors declare no conflict of interest.

References

1. Xiao, Z.; Xu, C.; Huang, Y.; He, X.; Shao, X.; Chen, Z.; Xie, C.; Li, T.; Xu, X. Analysis of spatial distribution of landslides triggered by the Ms 6.8 Luding earthquake in China on September 5, 2022. *Geoenviron. Disasters* **2023**, *10*, 3. [CrossRef]
2. Zhao, F.; Zhu, M.; Li, J.; Xu, Y.; Dan, C.; Xiao, Y.; Qiu, R.; Dong, J. Characteristics and Spatial Distribution of Highway Damage caused by the Ms 6.8 Luding Earthquake. *Res. Sq.* **2023**. [CrossRef]
3. Zhang, B.; Liu, G.; Wang, X.; Fu, Y.; Liu, Q.; Yu, B.; Zhang, R.; Li, Z. Semi-Automated Mapping of Complex-Terrain Mountain Glaciers by Integrating L-Band SAR Amplitude and Interferometric Coherence. *Remote Sens.* **2022**, *14*, 1993. [CrossRef]
4. An, Y.; Wang, D.; Ma, Q.; Xu, Y.; Li, Y.; Zhang, Y.; Liu, Z.; Huang, C.; Su, J.; Li, J.; et al. Preliminary report of the September 5, 2022 M_S 6.8 Luding earthquake, Sichuan, China. *Earthq. Res. Adv.* **2023**, *3*, 100184. [CrossRef]
5. Li, Y.; Zhao, D.; Shan, X.; Gao, Z.; Huang, X.; Gong, W. Coseismic Slip Model of the 2022 Mw 6.7 Luding (Tibet) Earthquake: Pre- and Post-Earthquake Interactions With Surrounding Major Faults. *Geophys. Res. Lett.* **2022**, *49*, e2022GL102043. [CrossRef]
6. Fu, Y.; Liu, Q.; Liu, G.; Zhang, B.; Zhang, R.; Cai, J.; Wang, X.; Xiang, W. Seasonal ice dynamics in the lower ablation zone of Dagongba Glacier, southeastern Tibetan Plateau, from multitemporal UAV images. *J. Glaciol.* **2021**, *68*, 636–650. [CrossRef]
7. Strozzi, T.; Luckman, A.; Murray, T.; Wegmuller, U.; Werner, C. Glacier motion estimation using SAR offset-tracking procedures. *IEEE Trans. Geosci. Remote Sens.* **2002**, *40*, 2384–2391. [CrossRef]
8. He, Z.; Li, Y.; Li, Y.; Sun, X.; Liu, D.; Ding, R.; Yang, P. The Surface Process and Seismogenic Structure of the 2021 Ms 6.1 Biru, Central Tibet Earthquake. *Seismol. Res. Lett.* **2022**, *93*, 1976–1991. [CrossRef]
9. Ma, J.; Yang, J.; Zhu, Z.; Cao, H.; Li, S.; Du, X. Decision-making fusion of InSAR technology and offset tracking to study the deformation of large gradients in mining areas-Xuemiaotan mine as an example. *Front. Earth Sci.* **2022**, *10*, 962362. [CrossRef]
10. Zhao, G.; Wang, L.; Deng, K.; Wang, M.; Xu, Y.; Zheng, M.; Luo, Q. An Adaptive Offset-Tracking Method Based on Deformation Gradients and Image Noises for Mining Deformation Monitoring. *Remote Sens.* **2021**, *13*, 2958. [CrossRef]
11. Xiao, R.; Jiang, M.; Li, Z.; He, X. New insights into the 2020 Sardoba dam failure in Uzbekistan from Earth observation. *Int. J. Appl. Earth Obs. Geoinf.* **2022**, *107*, 102705. [CrossRef]
12. Yang, Z.; Pang, B.; Dong, W.; Li, D. Spatial Pattern and Intensity Mapping of Coseismic Landslides Triggered by the 2022 Luding Earthquake in China. *Remote Sens.* **2023**, *15*, 1323. [CrossRef]
13. Zhou, S.; Sun, Z.; Sun, P. Rapid Glacier Shrinkage in the Gongga Mountains in the Last 27 Years. *Remote Sens.* **2022**, *14*, 5397. [CrossRef]
14. Huang, Y.; Xie, C.; Li, T.; Xu, C.; He, X.; Shao, X.; Xu, X.; Zhan, T.; Chen, Z. An open-accessed inventory of landslides triggered by the M_S 6.8 Luding earthquake, China on September 5, 2022. *Earthq. Res. Adv.* **2023**, *3*, 100181. [CrossRef]
15. Xu, S.; Fu, P.; Quincey, D.; Feng, M.; Marsh, S.; Liu, Q. UAV-based geomorphological evolution of the Terminus Area of the Hailuogou Glacier, Southeastern Tibetan Plateau between 2017 and 2020. *Geomorphology* **2022**, *411*, 108293. [CrossRef]
16. Zhang, L.; Fu, L.; Liu, A.; Chen, S. Simulating the strong ground motion of the 2022 M_S 6.8 Luding Earthquake, Sichuan, China. *Earthq Sci.* **2023**, *36*, 1–13. [CrossRef]
17. Zhong, Y.; Liu, Q.; Westoby, M.; Nie, Y.; Pellicciotti, F.; Zhang, B.; Cai, J.; Liu, G.; Liao, H.; Lu, X. Intensified paraglacial slope failures due to accelerating downwasting of a temperate glacier in Mt. Gongga, southeastern Tibetan Plateau. *Earth Surf. Dynam.* **2022**, *10*, 23–42. [CrossRef]
18. Liu, Q.; Zhang, B.; Zhao, B.; Zhong, Y.; Lu, X.; Zhou, J. Stability of the Hailuogou glacier during the "9.5" Luding Earthquake: A preliminary assessment based on multi-source observations. *J. Mt. Sci.* **2022**, *19*, 3037–3050. [CrossRef]
19. Guo, W.; Liu, S.; Xu, J.; Wu, L.; Shangguan, D.; Yao, X.; Wei, J.; Bao, W.; Yu, P.; Liu, Q.; et al. The second Chinese glacier inventory: Data, methods and results. *J. Glaciol.* **2017**, *61*, 357–372. [CrossRef]
20. Liu, J.; Hu, J.; Li, Z.; Ma, Z.; Wu, L.; Jiang, W.; Feng, G.; Zhu, J. Complete three-dimensional coseismic displacements due to the 2021 Maduo earthquake in Qinghai Province, China from Sentinel-1 and ALOS-2 SAR images. *Sci. China-Earth Sci.* **2022**, *52*, 882–892. [CrossRef]
21. Li, T.; Tang, X.; Zhou, X.; Zhang, X. LuTan-1 SAR Main Applications and Products. In Proceedings of the EUSAR 2022—14th European Conference on Synthetic Aperture Radar, Leipzig, Germany, 25–27 July 2022.
22. Liu, K.; Wang, R.; Zhang, H.; Liu, D.; Ou, N.; Chen, Y.; Yue, H.; Yu, W.; Deng, Y.; Liang, D.; et al. LuTan-1: An Innovative L-band Spaceborne SAR Mission. In Proceedings of the EUSAR 2022—14th European Conference on Synthetic Aperture Radar, Leipzig, Germany, 25–27 July 2022.
23. Lin, H.; Deng, Y.; Zhang, H.; Liu, D.; Liang, D.; Fang, T.; Wang, R. On the Processing of Dual-Channel Receiving Signals of the LuTan-1 SAR System. *Remote Sens.* **2022**, *14*, 515. [CrossRef]
24. Luckman, A.; Murray, T.; Jiskoot, H.; Pritchard, H.; Strozzi, T. ERS SAR feature-tracking measurement of outlet glacier velocities on a regional scale in East Greenland. *Ann. Glaciol.* **2003**, *36*, 129–134. [CrossRef]
25. Scambos, T.; Dutkiewicz, M.; Wilson, J.; Bindschadler, R. Application of image cross-correlation to the measurement of glacier velocity using satellite image data. *Remote Sens. Environ.* **1992**, *42*, 177–186. [CrossRef]
26. Li, J.; Li, Z.; Wu, L.; Xu, B.; Hu, J.; Zhou, Y.; Miao, Z. Deriving a time series of 3D glacier motion to investigate interactions of a large mountain glacial system with its glacial lake: Use of Synthetic Aperture Radar Pixel Offset-Small Baseline Subset technique. *J. Hydrol.* **2018**, *559*, 596–608. [CrossRef]

27. Zhang, Q.; Zheng, Y.; Zhang, L.; Li, Z.; Yan, S. South Inylchek Glacier Surface Motion Extraction and Analysis based on Time-series Pixel Tracking Algorithm. *Remote Sens. Technol. Appl.* **2020**, *35*, 1273–1282. [CrossRef]
28. Zhang, L.; Dai, K.; Deng, J.; Ge, D.; Liang, R.; Li, W.; Xu, Q. Identifying Potential Landslides by Stacking-InSAR in Southwestern China and Its Performance Comparison with SBAS-InSAR. *Remote Sens.* **2021**, *13*, 3662. [CrossRef]
29. Xiao, R.; Yu, C.; Li, Z.; Jiang, M.; He, X. InSAR stacking with atmospheric correction for rapid geohazard detection: Applications to ground subsidence and landslides in China. *Int. J. Appl. Earth Obs. Geoinf.* **2022**, *115*, 103082. [CrossRef]
30. Cheloni, D.; De Novellis, V.; Albano, M.; Antonioli, A.; Anzidei, M.; Atzori, S.; Avallone, A.; Bignami, C.; Bonano, M.; Calcaterra, S.; et al. Geodetic model of the 2016 Central Italy earthquake sequence inferred from InSAR and GPS data. *Geophys. Res. Lett.* **2017**, *44*, 6778–6787. [CrossRef]
31. Goldstein, R.M.; Werner, C.L. Radar interferogram filtering for geophysical applications. *Geophys. Res. Lett.* **1998**, *25*, 4035–4038. [CrossRef]
32. Massonnet, D.; Rossi, M.; Carmona, C.; Adragna, F.; Peltzer, G.; Feigl, K.; Rabaute, T. The displacement field of the Landers earthquake mapped by radar interferometry. *Nature* **1993**, *364*, 138–142. [CrossRef]
33. Chen, Y.; Yu, S.; Tao, Q.; Liu, G.; Wang, L.; Wang, F. Accuracy Verification and Correction of D-InSAR and SBAS-InSAR in Monitoring Mining Surface Subsidence. *Remote Sens.* **2021**, *13*, 4365. [CrossRef]
34. Li, Y.; Li, Y.; Liang, K.; Li, H.; Jiang, W. Coseismic Displacement and Slip Distribution of the 21 May 2021 Mw 6.1 Earthquake in Yangbi, China Derived From InSAR Observations. *Front. Environ Sci.* **2022**, *10*, 857739. [CrossRef]
35. Li, W.; Chen, J.; Lu, H.; Yu, C.; Shan, Y.; Li, Z.; Dong, X.; Xu, Q. Analysis of Seismic Impact on Hailuogou Glacier after the 2022 Luding Ms 6.8 Earthquake, China, Using SAR Offset Tracking Technology. *Remote Sens.* **2023**, *15*, 1468. [CrossRef]
36. Wang, X.; Fang, C.; Tang, X.; Dai, L.; Fan, X.; Xu, Q. Research on Emergency Evaluation of Landslides Induced by Luding Ms 6.8 Earthquake. *Geomat. Inf. Sci. Wuhan Univ.* **2022**, *15*, 25–35. [CrossRef]
37. Xu, J.; Shao, Z.; Ma, H.; Zhang, L. Evolution of Coulomb stress and stress interaction among strong earthquakes along the Xianshuihe fault zone. *Chin. J. Geophys.* **2013**, *56*, 1146–1158. [CrossRef]